Volume 26
Number 32
28 August 2024
Pages 21307–21916

PCCP

Physical Chemistry Chemical Physics

rsc.li/pccp

25 YEARS ANNIVERSARY

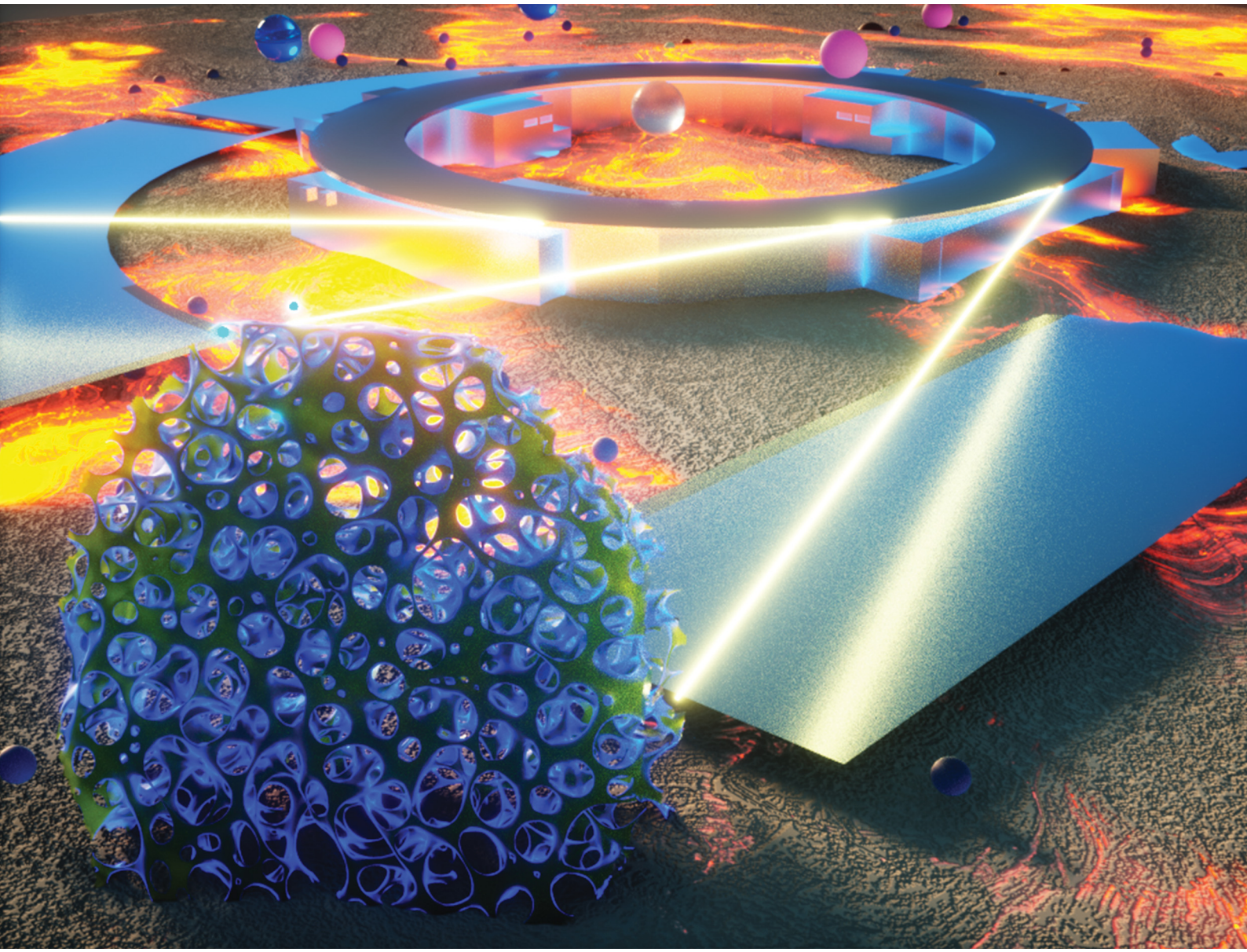

ISSN 1463-9076

ROYAL SOCIETY OF CHEMISTRY

PAPER

Vyacheslav S. Bryantsev, Anatoly I. Frenkel, Yu-chen Karen Chen-Wiegart *et al.*
Exploring Cr and molten salt interfacial interactions for molten salt applications

PCCP Owner Societies

PCCP

ROYAL SOCIETY OF CHEMISTRY

PAPER

View Article Online
View Journal | View Issue

Cite this: *Phys. Chem. Chem. Phys.*, 2024, **26**, 21342

Exploring Cr and molten salt interfacial interactions for molten salt applications†

Xiaoyang Liu,[a] Yang Liu,[a] Luke D. Gibson,[b] Mingyuan Ge,[c] Daniel Olds,[c] Denis Leshchev,[c] Jianming Bai,[c] Anna M. Plonka,[d] Phillip Halstenberg,[ef] Hui Zhong,[c] Sanjit Ghose,[c] Cheng-Hung Lin,[a] Xiaoyin Zheng,[a] Xianghui Xiao,[c] Wah-Keat Lee,[c] Sheng Dai,[ef] German D. Samolyuk,[g] Vyacheslav S. Bryantsev,[e]* Anatoly I. Frenkel[ad]* and Yu-chen Karen Chen-Wiegart[ac]*

Molten salts play an important role in various energy-related applications such as high-temperature heat transfer fluids and reaction media. However, the extreme molten salt environment causes the degradation of materials, raising safety and sustainability challenges. A fundamental understanding of material–molten salt interfacial evolution is needed. This work studies the transformation of metallic Cr in molten 50/50 mol% KCl–$MgCl_2$ *via* multi-modal *in situ* synchrotron X-ray nano-tomography, diffraction and spectroscopy combined with density functional theory (DFT) and *ab initio* molecular dynamics (AIMD) simulations. Notably, in addition to the dissolution of Cr in the molten salt to form porous structures, a δ-A15 Cr phase was found to gradually form as a result of the metal–salt interaction. This phase change of Cr is associated with a change in the coordination environment of Cr at the interface. DFT and AIMD simulations provide a basis for understanding the enhanced stability of δ-A15 Cr *vs.* bcc Cr, by revealing their competitive phase thermodynamics at elevated temperatures and probing the interfacial behavior of the molten salt at relevant facets. This study provides critical insights into the morphological and chemical evolution of metal–molten salt interfaces. The combination of multimodal synchrotron analysis and atomic simulation also offers an opportunity to explore a broader range of systems critical to energy applications.

Received 14th March 2024,
Accepted 13th May 2024

DOI: 10.1039/d4cp01122h

rsc.li/pccp

Introduction

The properties of a wide variety of materials in catalytic, chemical, electrochemical, solar, and nuclear energy applications are defined by the structure of solids at interfaces with strongly reactive media. These reactive solid–fluid interfaces are prevalent, ranging from nano-/meso-scale functional materials such as heterogeneous catalysts, batteries, solar cells, fuel cells and sensors to large-scale structural materials used in nuclear and solar power plants. For instance, in heterogeneous catalysts, the reconstruction of metal nanoparticle surfaces caused by the adsorbates exerts a strong influence on surface chemistry and catalytic activity.[1] Among the various reactive media, the effects of ionic liquids and molten salts on the surface restructuring phenomena at the interfaces with solid materials are of particular interest due to the strong sensitivity of the morphology, chemical compositions, and structure of solid materials at the interfaces.[2,3] Unique solid–liquid interfacial properties led to a range of applications, including tailoring the surface structure of heterogeneous catalysts,[4] mediating colloidal synthesis of nanomaterials,[5] creating gradient Li-rich oxide cathodes,[6] controlling surface bonds of 2D transition-metal carbides and nitrides (MXenes),[7,8] and playing key roles in modifying functional layers in perovskite solar cells.[9]

Similarly to ionic liquids, molten salts have been recognized for their strong potential as key components in materials for energy applications. They find uses in sustainable energy facilities and systems, such as molten salt reactors,[10–13] large-scale solar concentrated power plants,[14–16] energy storage,[6,17,18]

[a] *Materials Science and Chemical Engineering, Stony Brook University, Stony Brook, NY, USA. E-mail: Karen.Chen-Wiegart@stonybrook.edu, anatoly.frenkel@stonybrook.edu*
[b] *Computational Sciences and Engineering Division, Oak Ridge National Laboratory, Oak Ridge, TN, USA*
[c] *National Synchrotron Light Source II (NSLS-II), Brookhaven National Laboratory, Upton, NY, USA*
[d] *Chemistry Division, Brookhaven National Laboratory, Upton, NY, USA*
[e] *Chemical Sciences Division, Oak Ridge National Laboratory, Oak Ridge, TN, USA. E-mail: bryantsevv@ornl.gov*
[f] *Department of Chemistry, University of Tennessee, Knoxville, TN, USA*
[g] *Materials Science and Technology Division, Oak Ridge National Laboratory, Oak Ridge, TN, USA*

† Electronic supplementary information (ESI) available. See DOI: https://doi.org/10.1039/d4cp01122h

two-dimensional derivative MXenes,[7,19,20] electrolytes for molten salt batteries,[21–23] and porous materials,[24–27] due to their distinct advantages, including low vapor pressure, high specific heats, large operational temperature windows, and low cost.[28–30] When materials come into contact with molten salts, which can be regarded as high-temperature ionic liquids, the salt, in combination with elevated temperature, can induce and accelerate morphological, chemical, and structural changes. These interfacial changes between the materials and molten salt can profoundly impact various applications. For example, in CO_2 capture, the presence of molten salt increases the CO_2 uptake kinetics;[31,32] and when nanocomposites are suspended in molten salt to enhance heat storage and transfer properties for concentrated solar power systems, the solid–molten salt interfaces directly impact interfacial thermal transport, interfacial thermal resistance and thermal conductivity.[33]

Although the knowledge of interfacial structural and chemical changes, including their kinetics, at metal–reactant interfaces is of immense significance for achieving the rational design of functional materials and structural alloys, it remains challenging to comprehensively characterize the evolution of such interfaces. This is primarily because of the paucity of most interface-sensitive techniques to probe these changes *in situ*, under a rapidly evolving condition such as the extreme environment of molten salt under elevated temperatures. To overcome this limitation, we established a comprehensive investigation framework using Cr microparticles in molten KCl–$MgCl_2$ as a model system. A KCl–$MgCl_2$ mixture with a high boiling point and low cost is one of the promising heat transfer fluid candidates in concentrated solar power applications,[34,35] and has been used as a model system in studies for molten salt reactor applications.[27,36,37] We demonstrated that the use of microparticles can be an effective platform to create a large amount of interfaces interacting with the reactive fluid media. Employing a multimodal toolbox, we conducted *in situ* studies on the morphological, structural, and chemical evolution of the metal surface using synchrotron X-ray techniques including nano-tomography, absorption spectroscopy and diffraction, with their resolving power spanning various length and time scales. While the well-known phenomenon - dissolution of Cr due to salt impurities - was directly visualized in 3D, this study reveals the surface reordering of δ-A15 Cr from bcc Cr at the formed Cr–molten salt interface, resulting in a change in the Cr coordination environment in the molten salt during the initial stage of the reaction. By combining density functional theory (DFT) and *ab initio* molecular dynamics (AIMD) simulations, computational models were built to compare the stability of bcc and δ-A15 Cr and the interfacial behavior of the stable facets for different Cr phases with affinities for Mg^{2+}, K^+, and Cl^- ions. This approach revealed a unique sequence of phase transformations within the surface layers of the metal, shedding light on the underlying mechanisms and offering valuable insights and a characterization strategy that is applicable to a wide range of materials and their interactions with reactive media.

Results and discussion

The morphological evolution of Cr particles in molten KCl–$MgCl_2$

The 3D morphological change of Cr particles in 50/50 mol% KCl–$MgCl_2$ at 700 °C was studied using *in situ* synchrotron X-ray nano-tomography. Cr was chosen as an ideal model system because it can preferentially dissolve and subsequently lead to the degradation of alloys.[38] Many prior studies have evaluated the loss of Cr and void formation in Ni-based alloys, including Cr depletion distance,[39] mass change[40] and corrosion crack (pore) depth.[41,42] High-throughput analysis combined with machine learning, first-principles density functional theory (DFT), and CALPHAD modeling have been conducted to determine the dependencies of corrosion on the physical parameters in Cr–Fe–Mn–Ni alloys.[43] Fundamental studies using Ni-20Cr as a model alloy have been carried out to reveal void formation mechanisms in molten salt using synchrotron transmission X-ray microscopy and electron microscopy.[27,44–47] The stable chemical states and local coordination structures of Cr and Ni in molten salt related to corrosion and transport properties have also been studied *via* synchrotron X-ray scattering and spectroscopy in combination with *ab initio* molecular dynamics (AIMD) simulations at the atomic level.[48–51]

The morphology of the pristine Cr particle before reacting with the molten salt is shown in Fig. S2 (ESI†). The pristine Cr particle was solid with only a very small amount of initial internal voids. Fig. 1A and B show the surface and internal changes of the Cr particle in KCl–$MgCl_2$ at 700 °C in 3D. As the reaction time increased, small sub-micron particles (indicated by red arrows) formed around the original micron-sized Cr particle. It was also observed in the pseudo-2D *XY* cross-sectional views (Fig. 1C). The small particles were formed within a short amount of reaction time. The small particles then grew larger and connected into a layer surrounding the surface of the Cr particle (indicated by yellow arrows). To identify these small particles, which were not from the original Cr particle, Fig. 2D depicts the contour of the particles in the 2D *XY* images at the initial imaging time point (1.1 min) and the end of the reaction time point (73.0 min). The outline of the particle at 73.0 min was larger than that of 1.1 min indicating the surface layer was formed from the interaction of the Cr and the molten salt.

In addition, the dissolution of Cr in KCl–$MgCl_2$ was observed from the formation of pores in the Cr particle (Fig. 1B and C). Within a 1.1 min reaction time, some small pores were observed in the Cr particle (indicated by black arrows). With longer reaction time, more and larger pores appeared as shown in the X-ray nano-tomography results. The dissolution of Cr was consistent with previous work on Ni–Cr binary model alloys[44,46] and engineering Ni alloys[52,53] containing Cr, which was the result of anodic dissolution of Cr in molten salt. A previous study demonstrated $CrCl_3$ as the stable anodic reaction products in molten KCl–$MgCl_2$.[54] Purified KCl–$MgCl_2$ was used in the experiment, and a small amount of MgO and evolving HCl gas can form at 700 °C. Counter reduction of

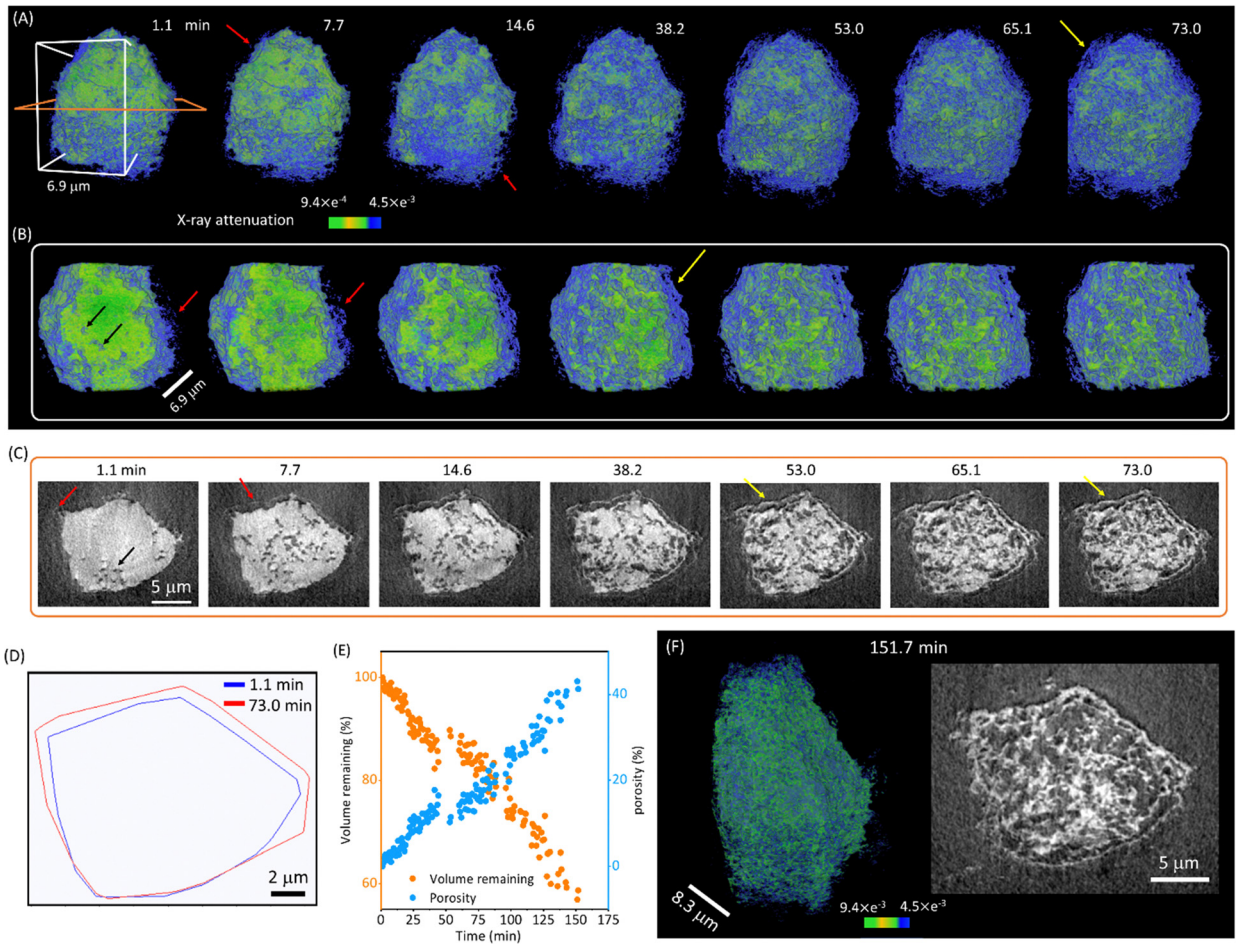

Fig. 1 Visualization and quantification from the *in situ* X-ray nano-tomography analysis showing the morphological change of the Cr particle in molten salt. (A) The 3D visualizations of the particle at selected time points showing the growth of particles on the surface layer. (B) The 3D visualizations and the pseudo-2D cross-sectional view of the Cr particle at the selected heating time points; both (B) and (C) show the pore formation from Cr dissolution in the particle. Red arrows indicate small particles growing outside of the original micro-particle; yellow arrows indicate the surface layer and black arrows indicate pores. (D) A contour comparison of the particle at the initial and the end of the reaction (1.1 and 73.0 min respectively) directly visualizes the growth of the surface layer in the molten salt. (E) The remaining volume of the Cr particle gradually decreased from the dissolution of Cr. (F) 3D and 2D views of the particle at 130.6 min reaction time showing more pores.

H^+ forming H_2 happens.[38] After a reaction time of ~150 min, the volume loss was ~40%, forming a highly porous structure (Fig. 1E). Fig. 1F shows the Cr particle at ~130.6 min. Overall, the morphological change shows: (1) dissolution of Cr in molten salt; and (2) growth of a surface layer from Cr in molten salt that did not undergo dissolution, suggesting that a new phase was formed as a result of the reaction with the molten salt.

The structure change of Cr in molten KCl–$MgCl_2$

To gain a better understanding of the crystalline structural change of the Cr in molten KCl–$MgCl_2$, *in situ* synchrotron XRD measurements were conducted at 700 °C. First, a control experiment was carried out to observe the structural change of Cr powder sealed in a quartz capillary (Ar environment) without salt at 700 °C. The integrated diffraction patterns of the control experiment as a function of the heating time at 700 °C are shown in Fig. 3A. The diffraction peaks were identified as bcc Cr. No changes were observed, which is consistent with the expectation that Cr does not undergo structural changes at 700 °C in an inert environment. Rietveld refinement was achieved using the *in situ* diffraction patterns (Fig. S4, ESI†) and showed that the lattice parameter of bcc Cr remained at 2.875 Å.

The time-resolved XRD patterns from the bcc Cr reacting in molten KCl–$MgCl_2$ (50–50 mol%) at 700 °C are shown in Fig. 2B. At the beginning of the experiment, the diffraction peaks were identified as bcc Cr, with the same peak positions as the control experiment shown in Fig. 2A. The intensity of the bcc Cr peaks corresponding to (110) at 4.7 deg (Fig. S5, ESI†), (200) at 6.6 deg, (211) at 8.1 deg and (220) at 9.4 deg (Fig. 2B) decreased immediately as the reaction started indicating that the amount of bcc Cr decreased in the molten salt. This is consistent with either the dissolution of Cr in molten KCl–$MgCl_2$, the formation of a new Cr phase, or a combination of these processes. The dissolution of Cr was observed using

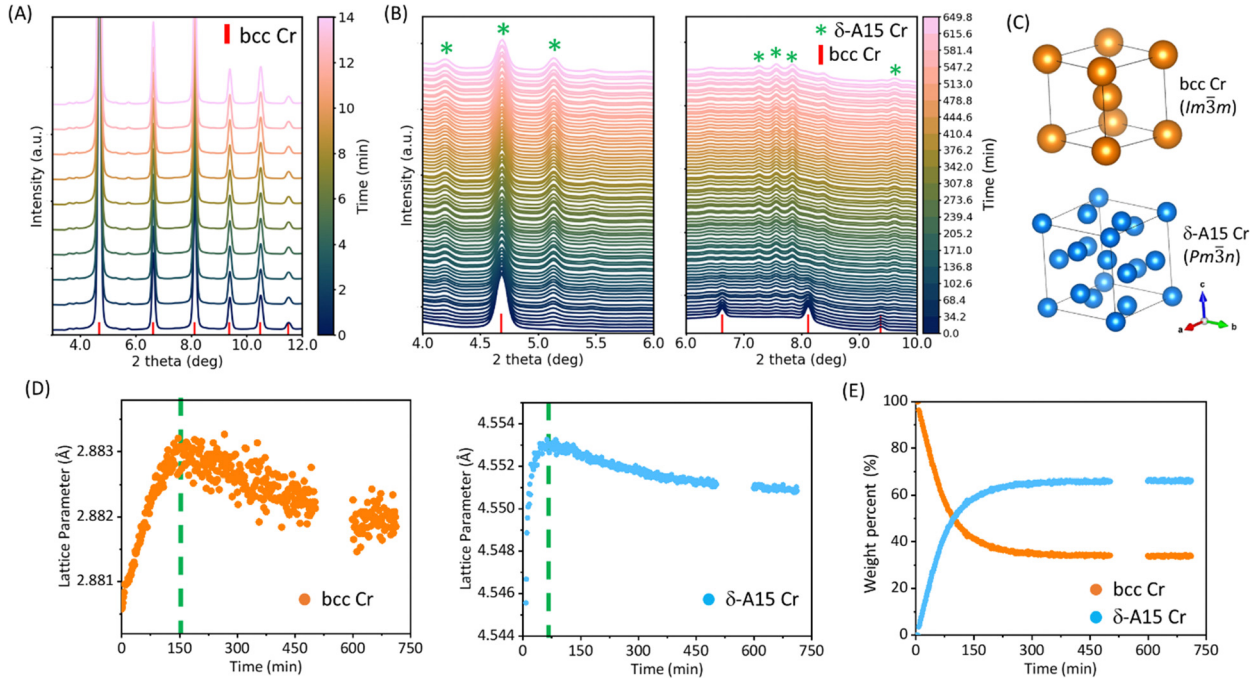

Fig. 2 The *in situ* X-ray diffraction (XRD) patterns for bcc Cr in Ar and KCl–$MgCl_2$ (50–50 mol%) at 700 °C. (A) The XRD pattern evolution of bcc Cr in Ar at 700 °C, which did not show changes. (B) The evolution of the XRD patterns from bcc Cr reacting in molten KCl–$MgCl_2$. The peaks were identified as bcc and δ-A15 Cr. (C) The crystal structures of bcc Cr and δ-A15 Cr. (D) The lattice parameter *vs.* reaction time for the fitted bcc and δ-A15 Cr phases during the *in situ* experiment, analyzed by Rietveld refinement. (E) The relative weight ratio *vs.* reaction time of bcc Cr and δ-A15 Cr.

in situ synchrotron X-ray nano-tomography (as shown in the previous section). Interestingly, at the same time, new peaks at 4.2, 5.1, 7.3, 7.6 and 7.8 deg appeared and gradually increased in intensity. These peaks were identified as δ-A15 Cr. Fig. 2C compares the crystal structure of bcc and δ-A15 Cr.

The presence of a δ-A15 Cr structure along with bcc Cr has been reported in the literature; for example, the δ-A15 Cr structure has been created by evaporation and condensation of Cr on a Cu grid in an Ar environment, characterized by electron microscopy.[55,56] Previous work has shown that bcc Cr could be transformed to δ-A15 Cr by single-pulse laser irradiation (60 ns; λ = 0.694 μm; 0.2 × 10^6 W cm^{-2}).[57] Further work also reported this δ-A15 structure in thin films,[58,59] fine particles[56,60] and nano-sized particles as a reduction product in lithium-ion batteries.[61,62] Our data suggested that δ-A15 Cr formed at the evolving Cr–molten salt interface. A coexistence of surface structural change and anodic dissolution of Cr occurred in molten salt. The formed interfacial δ-A15 Cr was stable in molten KCl–$MgCl_2$. Other small diffraction peaks at ~5.5 and 8.5 deg were observed during the reaction; however, they did not match with known possible structures. No crystalline $CrCl_3$ or $CrCl_2$ formed at 700 °C during this reaction, which suggests that these potential corrosion products, if present, were dissolved in the molten salt instead of forming solid crystals. Additionally, another possible phase, Cr_3Si, has an XRD pattern that is nearly identical to the δ-A15 Cr phase; and could have resulted from Si leached out of the quartz capillary. However, EXAFS modeling using the Cr–Si and Cr–Cr contributions from the known Cr_3Si structure did not result in a satisfactory fit to the data. Therefore, we concluded that δ-A15 Cr is the most probable phase.

Furthermore, Rietveld refinement was conducted on the *in situ* XRD patterns using the bcc and δ-A15 Cr structures to fit the lattice parameters and weight percentage. The representative fitting results are shown in Fig. S6 (ESI†). The changes in the lattice parameter of bcc and δ-A15 Cr phases as a function of the reaction time are shown in Fig. 2D. The lattice parameter of bcc Cr shows an increasing trend for the first 150 min of reaction, which was different from the constant lattice parameter (2.875 Å) of the control experiment. The increase of the lattice parameter suggests an increase of disorder for the bcc Cr in the molten salt. This is consistent with the dissolution of Cr, which created more Cr–salt interfaces and likely a higher extent of disorder at those interfaces. Since bcc Cr heated at 700 °C in the control experiment without the molten salt did not show a lattice parameter change, the slight increase of the bcc Cr lattice parameter in the molten salt was possibly from the larger surface area produced by the Cr–molten salt reaction, which could be less ordered.

As for δ-A15 Cr, the lattice parameter increased at the beginning of the experiment, but only continued to increase until ~75 min. The change might be from the initial stage of formation of δ-A15 Cr. After that, δ-A15 Cr was stable in the molten salt. Moreover, Fig. 2D shows the relative weight percentage evolution between the bcc Cr and δ-A15 Cr during the *in situ* reaction in molten salt. The relative fraction of bcc Cr decreased immediately and continuously to ~40 wt%, while the fraction of δ-A15 Cr increased to ~60 wt%. After that, with a

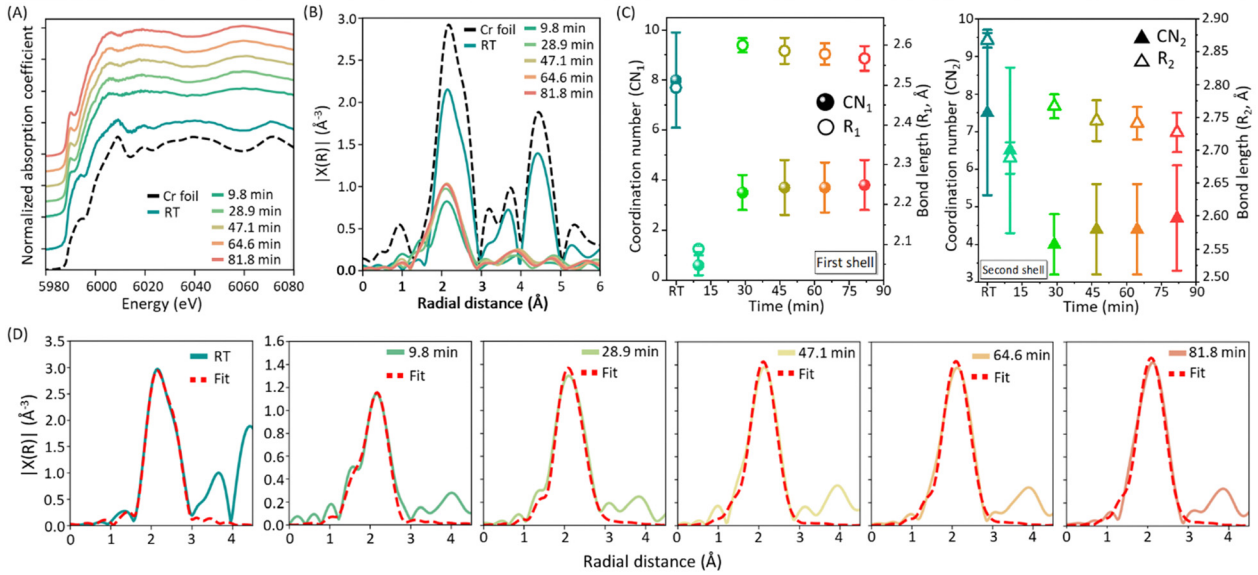

Fig. 3 The *in situ* XAS of bcc Cr in molten KCl–$MgCl_2$. (A) XANES spectra change along with the reaction time at 700 °C. (B) Fourier transform magnitude of the k^2-weighted EXAFS spectra. (C) The fitted coordination numbers (CN_1, CN_2) and bond lengths (R_1, R_2). (D) The best fit to the RT and *in situ* datasets with bcc and δ-A15 Cr models.

longer reaction time, the proportions did not change. One possible explanation of the incomplete dissolution of bcc Cr is the presence of a small number of impurities in the salt that could drive the corrosion reactions. After exhausting the limited oxidants in the molten salt, the corrosion would stop. Interestingly, during the rapid dissolution (corrosion) of bcc Cr, δ-A15 Cr did not undergo dissolution. That suggests that δ-A15 Cr is more stable compared to bcc Cr with respect to corrosion in 50/50 mol% KCl–$MgCl_2$.

The local structure of Cr in molten KCl–$MgCl_2$

In addition to the long-range crystalline ordering studied by the *in situ* XRD, the local atomic environment of Cr in molten KCl–$MgCl_2$ was studied by *in situ* XAS at the Cr K-edge. Fig. 3A and B show the Cr K-edge X-ray absorption near-edge structure (XANES) and Fourier transform magnitude of the extended X-ray absorption fine structure (EXAFS) in *k*-space (Fig. S7, ESI†) and *r*-space (Fig. 3C). Overall, the XANES spectrum of the room temperature sample was similar to that of metallic Cr foil, which is in the bcc phase.

However, at 700 °C, the pre-edge and post-edge features of the XANES spectra showed marked differences from those corresponding to bcc Cr measured at room temperature. Fig. S8 (ESI†) shows a direct comparison between bcc Cr measured at room temperature and reacted at 81.8 min. Since the XRD analysis above suggests the formation of the δ-A15 Cr phase, that phase was modeled to fit the EXAFS spectrum at 81.8 min, as shown in Fig. 4C. The best fitting results are summarized in Table 1. The first-shell and second-shell coordination numbers (CN_1, CN_2) and bond lengths (R_1, R_2) obtained from the fit to the RT data are similar to those in the Cr foil. However, after reacting at 700 °C for 81.8 min, the R_1 and R_2 values of the Cr–Cr bonds changed from 2.49 ± 0.01 Å and 2.87 ± 0.01 Å at RT to 2.57 ± 0.03 Å and 2.73 ± 0.03 Å, respectively, indicating a drastic transformation away from the bcc phase. The similarity between these R_1 and R_2 values and the δ-A15 Cr values (2.57 Å and 2.82 Å, respectively), together with the reduced values of CN_1 and CN_2 compared to their bulk δ-A15 Cr counterparts, indicate that the nanoscale, δ-A15- type Cr structure was formed. In that sample, the coordination numbers CN_1 and CN_2 (3.8 ± 1.0 and 4.7 ± 1.4) are lower than the bulk values (4 and 8, respectively) due to the finite surface to volume ratio,[63] consistent with the formation of pores from Cr dissolution. We note that these CNs are likely to be somewhat underestimated because the bond length disorder values (Table 1), also known as Debye Waller factors (DWFs), decrease with the time of exposure to the molten salt. That decrease is unexpected (for nanoscale materials, the disorder increases when the characteristic dimension decreases[64]) and is a very likely consequence of the correlation between the CNs and DWFs in the fitting process. Our analysis therefore provides their lower bounds, but it is still valuable for establishing evidence of the δ-A15 Cr phase.

The formation of δ-A15 Cr and phase stability comparison between bcc and δ-A15 Cr by DFT and AIMD simulation

Because polycrystalline Cr particles were used in this work, a non-uniform corrosion occurred that was similar to other work conducted on pure Cr foils[65] or Fe foils[66] in molten salt. As trace amounts of impurities are often present in molten salt, anodic dissolution of Cr could happen, forming Cr^{2+} or Cr^{3+}. A unique observation in the current work is the formation of δ-A15 Cr, which only occurred in the molten salt KCl–$MgCl_2$ and not in the control studies. It is possible that δ-A15 Cr was formed as a result of the interaction between bcc Cr and molten salt at the interface. Here, a surface reconstruction mechanism

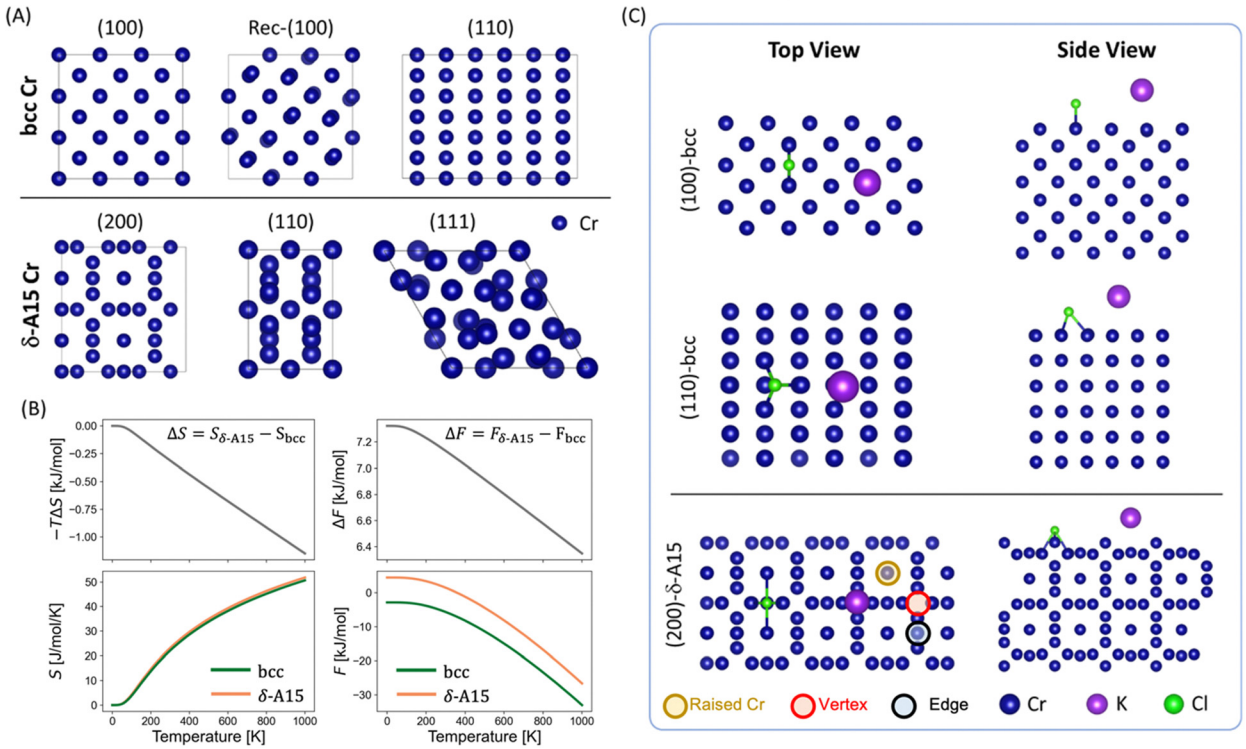

Fig. 4 Slab models for the surfaces of bcc and δ-A15 Cr and the phase thermodynamics. (A) Top view of three bcc surfaces - (100), rec-(100) and (110) and three δ-A15 surfaces – (200), (110) and (111). (B) Entropy and free energy comparisons between bcc and δ-A15 Cr as a function of temperature. (C) Top and side views of KCl adsorption structures on (100)-bcc, (110)-bcc and (200)-δ-A15 Cr. The three unique adsorption sites on (200)-δ-A15 Cr are marked in the top view of the surface in (C) with their corresponding labels at the bottom of the figure.

Table 1 Summary of the EXAFS fitting results of the sample at the room temperature (RT) before heating and after reacting for different time intervals at 700 °C. The Cr bcc structure was used to fit the RT data. The δ-A15 Cr structure was used to fit the 81.8 min data. Two Cr–Cr paths were used to fit the data.[56] The σ^2 values for the first and the second paths were constrained to be the same in the fits

Sample	CN_1	R_1, Å	CN_2	R_2, Å	σ^2, Å^2
Cr foil	8	2.520	6	2.910	—
δ-A15 Cr	4	2.571	8	2.817	—
RT	8.0 ± 1.9	2.494 ± 0.011	7.5 ± 2.2	2.867 ± 0.011	0.006 ± 0.002
9.8 min	0.6 ± 0.4	2.089 ± 0.007	6.5 ± 2.2	2.688 ± 0.024	0.010 ± 0.004
28.9 min	3.5 ± 0.7	2.600 ± 0.018	4.0 ± 0.8	2.767 ± 0.018	0.000 ± 0.003
47.1 min	3.7 ± 1.1	2.586 ± 0.033	4.4 ± 1.2	2.745 ± 0.031	0.002 ± 0.004
64.6 min	3.7 ± 1.0	2.578 ± 0.027	4.4 ± 1.2	2.741 ± 0.025	0.002 ± 0.004
81.8 min	3.8 ± 1.0	2.567 ± 0.031	4.7 ± 1.4	2.727 ± 0.030	0.001 ± 0.004

at the Cr–salt interface due to corrosion is proposed. Corrosion on bcc Cr created new interfaces with high surface energy, leading to surface reconstruction to reduce energy and stabilize the interfaces. To understand the relative stability of bcc and δ-A15 Cr at a molten salt interface, computational simulations were conducted and are discussed below.

First, DFT calculations were conducted to consider the different facets of bcc Cr and δ-A15 Cr in vacuum. For bcc Cr, Cr adopts an antiferromagnetic (AFM) arrangement of spins in its lowest energy state. However, there was no stable AFM arrangement for the δ-A15 Cr structure, in agreement with what we expect from a temperature-independent paramagnetic phase.[67] Including zero point energies, the bcc Cr was computed to be more stable than the δ-A15 Cr at T = 0 K (–926.0 *vs.* –918.6 kJ mol^{-1} per Cr atom, respectively).

The slab models of each surface were generated for bcc and δ-A15 Cr, with details shown in Table 2. Top-down views of each surface can be seen in Fig. 4A. For the bcc Cr phase, the (100) surface exhibited a marginally lower surface energy at 3.09 J m^{-2}. For all bcc slabs, both ferromagnetic (FM) and AFM arrangements were attempted, but only the AFM arrangement was successfully converged. Calculated surface energies for the (100) and (110) facets of AFM bcc Cr are consistent with previous calculations.[68] Nonmagnetic (NM) calculations were also performed to approximate the paramagnetic system at temperatures above chromium's Néel temperature (T_N = 310 K).[69]

Table 2 System descriptions and surface energies for bcc and δ-A15 Cr slab systems. KCl adsorption energies on bcc and δ-A15 Cr surfaces computed using eqn (2). NM represents nonmagnetic and AFM represents antiferromagnetic

Facet	No. of Cr atoms	Magnetism	No. of unit cells in the supercell surface	*k*-points	Surface energy [J m^{-2}]
bcc Cr					
(100)	108	AFM	3 × 3	6 × 6 × 1	3.09
(100)	108	NM	3 × 3	6 × 6 × 1	3.53
(110)	108	AFM	3 × 3	6 × 6 × 1	3.11
(110)	108	NM	3 × 3	6 × 6 × 1	3.19
δ-A15 Cr					
(200)	84	NM	2 × 2	6 × 6 × 1	3.17
(110)	42	NM	1 × 1	12 × 12 × 1	3.50
(111)	69	NM	1 × 1	12 × 12 × 1	3.57
KCl adsorption energies on bcc and δ-A15 Cr					
(100)-bcc	144	AFM	3 × 6	6 × 4 × 1	−145.9
(100)-bcc	144	NM	3 × 6	6 × 4 × 1	−164.0
(110)-bcc	144	AFM	3 × 4	6 × 6 × 1	−232.4
(110)-bcc	144	NM	3 × 4	6 × 6 × 1	−228.1
(200)-δ-A15	168	NM	2 × 4	6 × 3 × 1	−225.0

Justification for approximating paramagnetic Cr as a nonmagnetic material is discussed in the ESI.† The (100) surface optimized to a reconstructed surface configuration [rec-(100)][70] in a zig-zag structure when spin-polarization was not enabled, whereas the AFM (100) surface did not undergo this kind of reconstruction. As for δ-A15 Cr, the (200) surface exhibited the lowest surface energy, closely approaching that of bcc Cr surfaces.

Furthermore, the vibrational entropy and free energy were computed by performing phonon calculations for bcc and δ-A15 Cr, as shown in Fig. 4B. At all temperatures, the δ-A15 phase exhibits larger vibrational entropy and thus is more favorable entropically than the bcc phase. However, the entropic gains of δ-A15 would not overcome the enthalpic stability of bcc (7 kJ mol^{-1} per Cr atom) until much higher temperatures, likely above the melting point of Cr. However, it ultimately lowers the difference in free energy by ∼1 kJ mol^{-1} per Cr atom at 1000 K. Furthermore, the difference in energy between the two phases shrinks by 1.5 kJ mol^{-1} per Cr atom with the loss of magnetic ordering in bcc above chromium's Néel temperature (*i.e.*, nonmagnetic bcc is more stable than δ-A15 by 5.8 kJ mol^{-1} per Cr atom). Both factors diminish the difference in the stability between the two phases with increasing temperature, but do not overcome the higher thermodynamic stability of the bcc phase at the experimentally accessible temperature range.

Consequently, the influence of a salt component – KCl on the stability of bcc and δ-A15 Cr was studied by computing the single KCl ion pair adsorption energies for (100)-bcc, (110)-bcc and (200)-δ-A15 Cr as listed in Table 2. To model the loss of magnetic ordering at elevated temperatures for the bcc surfaces, NM calculations were also performed. The above facets were chosen due to their greater stability over other facets and thus they are more likely to be present in physical systems. The most favorable adsorbed structure of a single KCl at each surface is shown in Fig. 4C (top and side views). For bcc Cr, the (100) and (110) facets exhibit a large disparity in their adsorption energies, which implies that the (110) facet may become more prevalent than the (100) facet in molten KCl, despite the similar surface energy of (100) in vacuum. The adsorption energy of KCl on the (200) facet of δ-A15 Cr (−225.0 kJ mol^{-1}) was comparable to the strong adsorption on (110)-bcc Cr (−228.1 kJ mol^{-1}) and significantly larger than on (100)-bcc Cr (−164.0 kJ mol^{-1}), which suggests that (200)-δ-A15 Cr is competitive with (110)-bcc Cr. The weaker adsorption of KCl on (100)-bcc compared to the other two surfaces is likely due to the lower coordination of Cl^- with surface Cr atoms. The (100)-bcc Cr surface has the lowest density of surface Cr atoms (12.2 Cr atoms per nm^2) while (110)-bcc and (200)-δ-A15 Cr surfaces have surface densities of 17.2 and 19.4 Cr atoms per nm^2, respectively. This can also be observed in Fig. 4C, where only two bonds exist between Cl^- and Cr on (100)-bcc Cr, but the (110)-bcc and (200)-δ-A15 Cr surfaces exhibit three and four bonds, respectively. In summary, the thermodynamic simulation in this work first implies that, at 700 °C, the difference in free energy between bcc and δ-A15 Cr was reduced because δ-A15 Cr exhibited increasing entropy, while bcc Cr lost stabilizing effects from AFM arrangements as it transited into a paramagnetic material. Moreover, δ-A15 Cr showed a competitive affinity for molten KCl compared to (110)-bcc Cr.

Given the strong adsorption energetics for KCl on (110)-bcc and (200)-δ-A15 Cr surfaces, we performed AIMD simulations to better understand how molten 50/50 mol% KCl–$MgCl_2$ interacts with the two surfaces. The equilibration of each system was assessed using block averaging of the potential energies (Fig. S3, ESI†) and is discussed in greater detail in the ESI.† Snapshots of the two systems are shown in Fig. 5A, where the blue highlighted regions denote the atoms that are frozen during the simulation. Averaged over the last 7 ps of both AIMD simulations, probability density profiles for each ion in the melt along the surface normal direction were constructed (Fig. 5B). Mg^{2+} and Cl^- are clearly preferred at the interface for the (110)-bcc and (200)-A15 Cr surfaces, whereas K^+ favors the bulk region with no obvious structure. This is likely due to the strong inducement of mirror charges by Mg^{2+} at the Cr interfaces, as well as the high polarizability of Cl^- compared to K^+. The 0-point on the *x*-axis in Fig. 5B was set to the average *z*-coordinate of the top-most Cr atoms in both surfaces. Mg^{2+} and Cl^- appear to approach the (200)-δ-A15 surface more closely than (110)-bcc; however, this is convoluted by the higher

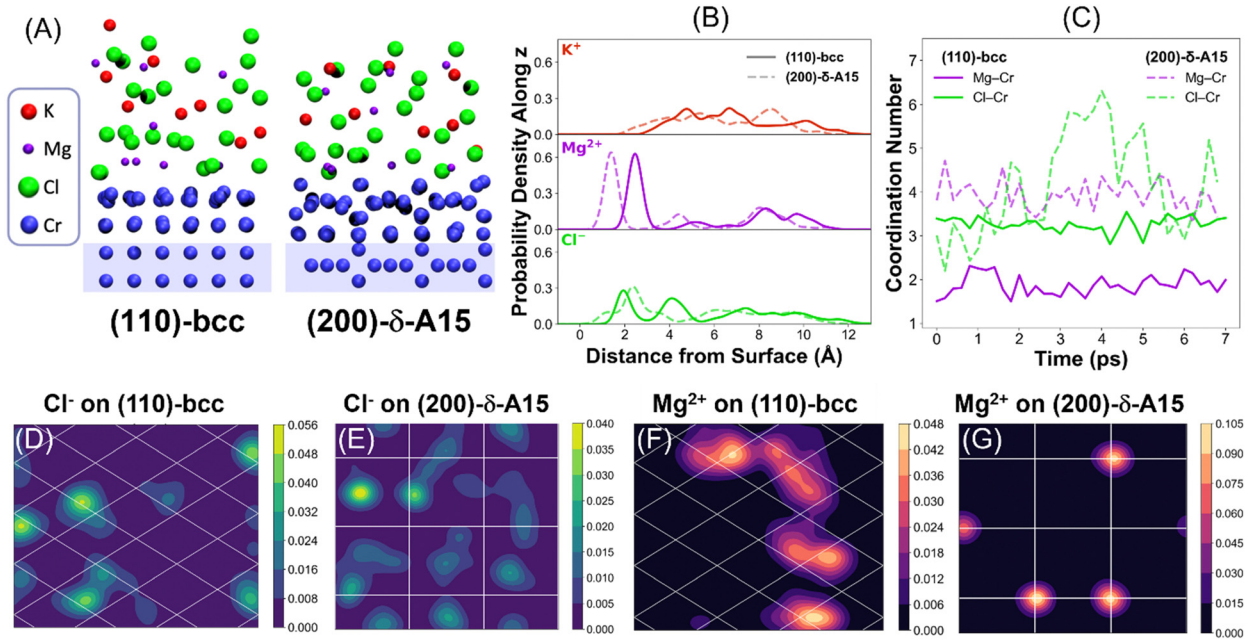

Fig. 5 Analysis of AIMD simulations. (A) Snapshots of the KCl–$MgCl_2$ mixture on each Cr surface. The blue highlighted region in the slab indicates the atoms that are frozen during AIMD. (B) Probability density profiles along the surface normal direction for K^+, Mg^{2+}, and Cl^- ions on the (110)-bcc and (200)-δ-A15 Cr surfaces. Heat maps are shown for interfacial Cl on (D) (110)-bcc and (E) (200)-δ-A15 Cr surfaces as probability densities. Heat maps are also shown for interfacial Mg^{2+} on (F) (110)-bcc and (G) (200)-δ-A15 Cr surfaces. For panels (D)–(G), atoms within 3 Å of the surface are considered interfacial atoms and the grid lines indicate the underlying structure of surface Cr atoms in each slab.

degree of surface roughness for (200)-δ-A15, which places a small number of Cr atoms above the rest of the surface (*i.e.*, raised Cr in Fig. 4C). The shapes of each profile were compared in 3 ps block averages, and they confirm that the interfacial regions are invariant. Due to the limited timescales, the regions beyond the interface were still fluctuating; however, the focus of this work is on the interfacial behavior of the KCl–$MgCl_2$ melt.

There is little difference between the shapes of the two Mg^{2+} profiles at the interfacial region, but Mg^{2+} on (200)-δ-A15 Cr does still approach the interface more closely than on (110)-bcc Cr despite the roughness of (200)-δ-A15. The Cl^- profiles, however, show two fundamentally different interfacial structures, largely attributed to the greater roughness of (200)-δ-A15 Cr. To clarify the interfacial behavior at the two surfaces, we constructed heat maps of Mg^{2+} and Cl^- positions at the surface using probability densities in Fig. 6D–G. Heat maps provide a valuable perspective for understanding the degree of localization and lateral mobility of interfacial ions at each surface. The grid lines in Fig. 5D–G indicate the underlying structure of the surface Cr atoms to provide a spatial reference.

Fig. 5D and E show probability densities of Cl^- at the surfaces of (110)-bcc and (200)-δ-A15 Cr, respectively. The lateral mobility (*i.e.*, spread of probability density) on both surfaces is similar, but given the complex interfacial structure of Cl^- at the (200)-δ-A15 Cr surface mentioned previously, it is difficult to directly compare with the heat map for the (110)-bcc Cr surface as the number of interfacial Cl^- ions differ in Fig. 5D and E. The disparity in ion mobility between the two surfaces is best seen in the Mg^{2+} heat maps (Fig. 5F and G). On (200)-δ-A15 Cr, Mg^{2+} ions are very securely adsorbed to the vertex sites and exhibit very little lateral mobility. On (110)-bcc Cr, Mg^{2+} ions have a much broader spread of probability density around their adsorption sites, suggesting greater surface diffusivity than on (200)-δ-A15 Cr.

To further understand the variations in ion–surface interactions between (110)-bcc and (200)-δ-A15 Cr, we also analyzed the average coordination number of Mg^{2+} and Cl^- with surface Cr atoms (Fig. 5C), the definition of which is given in the ESI.† Interestingly, the coordination numbers of Mg^{2+} and Cl^- with Cr on (200)-δ-A15 Cr (dashed lines, Fig. 5C) are on average higher than on (110)-bcc Cr (solid lines, Fig. 5C). Mg^{2+} coordination numbers for both surfaces are stable, but Mg^{2+} coordination on (200)-δ-A15 Cr is double that of (110)-bcc Cr values. Cl^- adsorption on (200)-δ-A15 displays much larger variance than the other curves in Fig. 5C due to the heterogeneity of the (200)-δ-A15 surface, where surface diffusion across short distances can cause a relatively large change in the number of nearby Cr surface atoms. The highly localized adsorption of Mg^{2+} at the vertex sites (Fig. 5G) and the overall increased coordination on (200)-δ-A15 Cr may indicate more favorable interfacial interactions between the melt and the (200)-δ-A15 Cr surface. In conjunction with the phase thermodynamics presented above, these factors provide support for the relative stabilization and appearance of the δ-A15 Cr phase in contact with molten KCl–$MgCl_2$. While this finding is largely qualitative, it also lays the foundation for future studies into the atomistic driving forces behind the formation of this unexpected δ-A15 Cr phase.

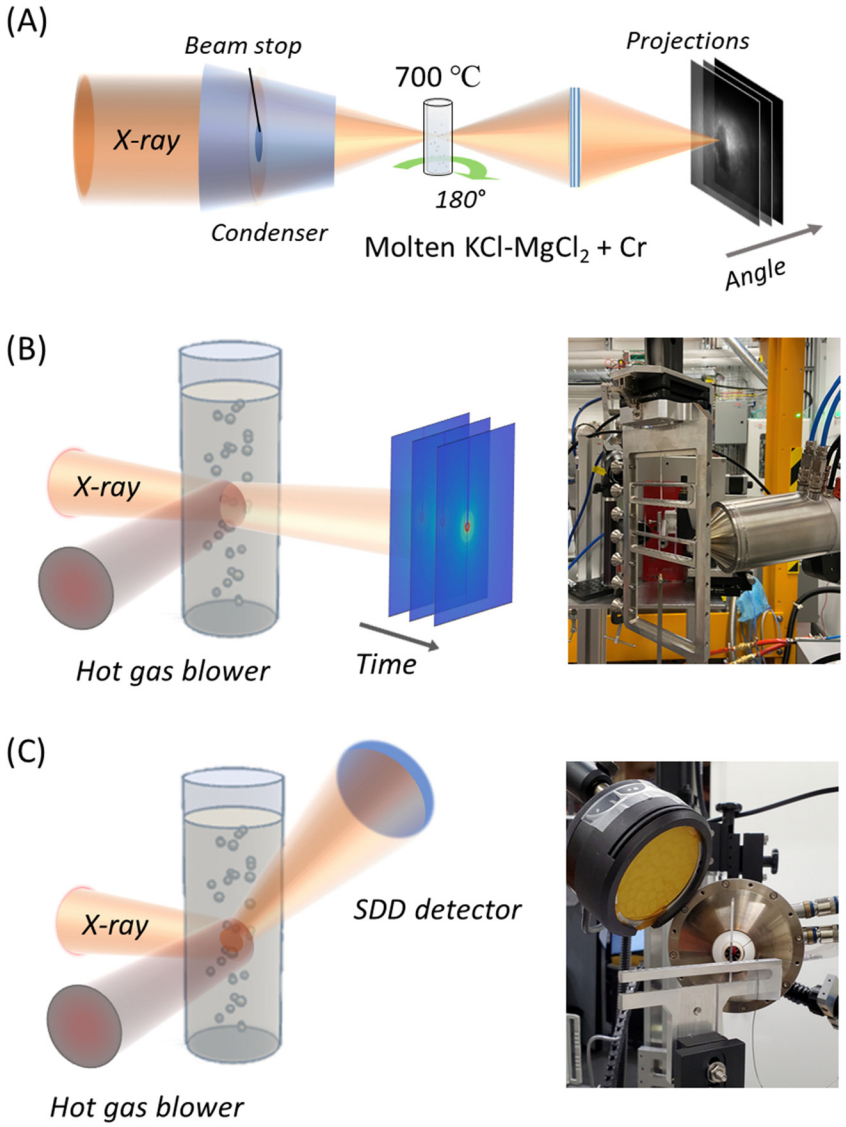

Fig. 6 Schematic of the multimodal synchrotron characterizations for *in situ* experiments of: (A) X-ray nano-tomography with transmission X-ray microscopy (18-ID, FXI beamline), (B) X-ray powder diffraction (28-ID-1, PDF beamline) and (C) X-ray absorption spectroscopy (8-ID, ISS beamline). All beamlines are at the NSLS-II, BNL.

Additionally, since *in situ* synchrotron X-ray nano-tomography observed the formation of small particles and their connection into a surface layer, the radiolytic effects of the X-rays may need to be considered. Previous work has shown X-ray induced Ni nanoparticle formation from $NiCl_2$ in molten $ZnCl_2$.[8] Thus, there could be two origins for the δ-A15 Cr phase accumulation observed in molten 50/50 mol% KCl–$MgCl_2$: (1) structural rearrangement of the bcc phase to δ-A15 in existing Cr particles, perhaps assisted by the destabilizing effects of corrosion, and (2) formation of δ-A15 Cr particles by X-ray-driven reduction of dissolved Cr^{2+} and Cr^{3+}.

Methods

In situ synchrotron sample preparation

Preparation of the 50/50 mol% KCl–$MgCl_2$ salt mixture was performed as detailed in previous work.[27,45] Taking advantage of the different vapor pressures of $MgCl_2$, its oxides and hydroxychlorides, the $MgCl_2$ was purified *via* fractional distillation starting from commercial anhydrous salt. The KCl (99.999% Suprapur reagent grade) and purified $MgCl_2$ were ground, mixed and pre-melted at 600 °C in the glovebox. Quartz capillaries were baked in a box furnace at 500 °C for ~45 min to remove potential organic contamination, then in an oven at 120 °C for at least 3 h to remove any surface moisture and stored immediately in the glovebox.

To prepare the samples for *in situ* experiments conducted at the inner-shell spectroscopy (ISS, 8-ID) and pair distribution function (PDF, 28-ID-1) beamlines at national synchrotron light source – II (NSLS-II) at Brookhaven National Laboratory (BNL), 5 wt% Cr powder (3 μm, 99.5%, US Research Nanomaterials, Inc) was mixed with KCl–$MgCl_2$ (50/50 mol%). The mixed powders were then loaded into capillaries with 0.7- and 1.5-mm

outer diameters (OD) for measurements at PDF and ISS beamlines, respectively. Additionally, pure Cr powder was loaded into a capillary (0.7 mm OD) as a control sample without salt for measurement at the PDF beamline. The PDF samples were put into 1.5 mm quartz capillaries (Fig. S1, ESI†). Each of the ISS and PDF samples was attached to a Swagelok fitting with a closed valve and then transferred out of the glovebox. The sample with the Swagelok fitting was then connected to and evacuated with a mechanical vacuum pump for ~5–10 min with the valve open. After that, the valve was closed again. Finally, the sample with the closed valve fitting was flame-sealed using a miniature benchtop hydrogen torch (Rio Grande) to ensure closure of the capillary. The sample was not exposed to air after being taken out of the glovebox.

To prepare the samples for the *in situ* experiment at full field X-ray Imaging (FXI, 18-ID) at NSLS-II, BNL with sufficient X-ray transmission, a double-capillary design was used, similar to the methods developed for micro-wires in our prior work.[27,44] Here, Cr powder was first added into a small quartz capillary (0.1 mm diameter), while the molten KCl–$MgCl_2$ was drawn up into the powder-filled capillary by a syringe using the capillary as a syringe tip. This inner capillary containing the powder in the salt was then placed into a larger (1.0 mm diameter) quartz capillary to ensure appropriate sealing of the samples. After the FXI samples were taken out of the glovebox, the outer capillaries were immediately flame-sealed using the mini-torch system.

Synchrotron characterizations and data analysis

In situ X-ray nano-tomography

The sample was mounted onto a TXM sample holder and heated in a miniature furnace integrated with the TXM at the FXI beamline.[71] The experimental setup is shown in Fig. 6(A). The sample was heated with a ramp rate of 25 °C min^{-1} and then held at 700 °C during the *in situ* X-ray tomography measurements. The X-ray incident energy was 9.8 keV for an optimal imaging contrast for the Cr particles. The images were captured under a camera binning of 2, providing a field of view of 55.5 × 46.8 μm^2 ($h \times v$) and an effective pixel size of 43.34 nm in this study. Each tomographic scan was taken by collecting 2D projections over a complete angular range of 180° with an exposure time of 0.04 seconds per 2D projection, which took ~ 1 min per full 3D tomographic measurement. The collected tomographic datasets were then reconstructed using the reconstruction modules in Tomopy.[72]

The 3D tomographic reconstruction stack images were cropped into volumes of 28.6 μm × 27.7 μm × 30.3 μm (height). A batch segmentation of the solid and pore phases was applied using a Python script based on the thresholding value between the characteristic peaks in the histogram of pixel values in the 3D images. The threshold value was determined from a representative scan and then the same value was applied to all scans. The visualization of 2D virtual cross-sectional images and 3D morphological evolution was conducted using commercial software Avizo (Thermo Fisher Scientific, v9.3).

In situ X-ray diffraction

A hot air blower (FMB Oxford) was used to heat the samples (Fig. 6B). The temperature of the heater was calibrated using standard CeO_2 powder in a quartz capillary before the experiment. A two-dimensional (2D) amorphous silicon-based flat panel detector (PerkinElmer) with a pixel size of 200 × 200 μm^2 was mounted orthogonally to the X-ray beam to collect the diffraction rings in transmission mode (Fig. 6B). The wavelength of the incident X-ray was 0.1665 Å (74.46 keV), and the sample-to-detector distance was calibrated by using a Ni standard and calculated to be 245.05 mm. The exposure time of each scan was 30 seconds per 2D diffraction pattern. The hot air was preheated to 700 °C before the *in situ* PDF experiment. The data collection started after the sample was moved to the X-ray beam position, which was pre-heated to 700 °C by the hot gas blower and calibrated.

The diffraction rings in each 2D image were azimuthally integrated and reduced to an intensity *vs.* 2θ (diffraction angle) plot *via* a Python-based open-source program DIOPTAS (version 0.5.0).[73] The phases in the sample were compared with references in a commercial database PDF-4+ 2021 (JCPDS-ICDD). The Rietveld refinements were conducted subsequently using commercial software TOPAS (Bruker, Academic V6) to quantify the real-time evolution of the lattice parameter and the weight percentage of each phase from the *in situ* XRD measurements.

In situ hard X-ray absorption spectroscopy (XAS)

The same hot air blower as used for the *in situ* XRD experiment was used to heat the samples to 700 °C for the *in situ* XAS experiment of the Cr K-edge conducted at the ISS beamline. A similar protocol was followed, in which the heater was first pre-heated to the target temperature of 700 °C, and the XAS data collection started immediately after the sample was moved to the beam position. The *in situ* XAS spectra were recorded at the Cr K-edge from the Cr in the molten KCl–$MgCl_2$ sample in fluorescence mode with a 4-element silicon drift detector (SDD). The scanning and data acquisition time was ~3 min per spectrum. Five consecutive spectra were averaged to improve the signal to noise ratio.

X-ray absorption coefficient data were edge-step normalized and the isolated atom background was subtracted using the Athena program, which is part of the Demeter software package.[74] Fluorescence data exhibited a self-absorption effect that was corrected by multiplying the EXAFS spectra by a factor of 1.35. This constant scaling factor was obtained by comparing the transmission and fluorescence data from the same sample.[75] The data were fit using the FEFF6 theory for calculating photoelectron scattering amplitudes and phase shifts. The passive electron reduction factor, $S_0^2 = 0.72$, was obtained from fitting the Cr foil EXAFS spectrum. Two models of the Cr structure were considered for the fits: the body-center cubic (bcc) and the δ-A15 models.[55,56]

Surface energies and phase stabilities calculations

The KCl adsorption energies on various surface structures, including (100)-bcc, (110)-bcc and (200)-δ-A15 Cr, were computed by DFT calculations, performed using the Vienna *ab initio* simulation package (VASP, version 6.2.1).[76–79] The gradient-corrected functional of Perdew–Burke–Ernzerhof (PBE)[80,81] was employed, which has previously been shown to accurately describe the ground state properties of chromium.[82–86] While the PBE functional generally underestimates band gaps due to self-interaction error,[87] the system studied herein—Cr metal (no band gap) and molten $MgCl_2$–KCl (very high band gap)—is largely unaffected by this deficiency. However, the effects of self-interaction error would need to be addressed for systems containing narrow band gaps (*e.g.*, transition metal ions dissolved in molten salt) using methods such as DFT+U[88,89] or Perdew–Zunger self-interaction correction.[87,90] A detailed method for the calculations is described in ESI.† The surface energies were computed using the following equation,

$$E_{\text{surf}} = \frac{E_{\text{slab}} - N\,E_{\text{bulk}}}{2A} \quad (1)$$

where E_{slab} is the total energy of the optimized slab, N is the number of chromium atoms in the slab, E_{bulk} is the energy per chromium atom in either bcc or δ-A15 Cr phases, and A is the surface area of the slab system. Phonon calculations were performed for bcc and δ-A15 Cr bulk systems to estimate temperature-dependent thermodynamic quantities such as the vibrational entropy and free energy using the phonopy code.[91] The adsorption energies for a KCl ion pair on relevant surfaces of bcc and δ-A15 Cr were computed herein using the following equation,

$$E_{\text{ads}} = E_{\text{slab}}^{\text{KCl}} - E_{\text{slab}}^{\text{Vac}} - E_{\text{KCl}}^{\text{Vac}} \quad (2)$$

where $E_{\text{slab}}^{\text{KCl}}$ is the energy of the slab with KCl adsorbed onto the surface, $E_{\text{slab}}^{\text{Vac}}$ is the energy of the optimized surface in vacuum, and $E_{\text{KCl}}^{\text{Vac}}$ is the energy of a KCl contact ion pair in vacuum. Multiple placements of ions were tested for each surface and the most stable configurations are reported herein. K^+ and Cl^- ions were confirmed to have negligible spin densities in spin-polarized calculations. The KCl adsorption energies for (100)-bcc, (110)-bcc and (200)-δ-A15 Cr were then computed.

AIMD simulations were performed on two Cr surfaces [(110)-bcc and (200)-δ-A15 Cr] with a 50–50 mol% mixture of KCl and $MgCl_2$ (40 atoms total representing the molten salt) in the NVT ensemble. The temperature was maintained at 1000 K by the Nosé–Hoover thermostat and a time step of 1 fs was used. To facilitate faster calculations necessary for AIMD, the (110)-bcc and (200)-δ-A15 Cr slab surface models were thinner than those used in static DFT calculations and the lower halves of each slab were frozen in place to prevent unphysical reconstruction during AIMD simulations. A k-point mesh grid of $1 \times 1 \times 1$ was employed for both AIMD simulations. The surface areas of the (110)-bcc and (200)-δ-A15 Cr slabs were 12.15×11.45 Å^2 and 13.6×13.6 Å^2, respectively. For both surfaces, nonmagnetic states were adopted to better mimic the paramagnetic states that are expected at elevated temperatures, which is discussed below. A 2 nm vacuum layer was also placed above the molten salt to limit interactions with adjacent images. For both surfaces, simulations were equilibrated for 5 ps followed by 7 ps of production run used for analysis.

Conclusion

This work studies the interactions between Cr and molten KCl–$MgCl_2$ including morphological, structural, and chemical changes of Cr. To elucidate and bridge the changes occurring at different length scales, *in situ* multi-modal synchrotron X-ray nano-tomography, diffraction and spectroscopy were applied, combined with DFT and AIMD simulations. Micron-sized Cr particles were an ideal platform for this kind of correlative study, revealing the time-resolved transformation of the Cr structure at the interface with molten KCl–$MgCl_2$. The dissolution of Cr formed pores and nanoparticle accumulation as a surface layer around the original Cr particle. In addition to the dissolution of bcc Cr in molten KCl–$MgCl_2$, the δ-A15 Cr phase was formed. While both bcc and δ-A15 Cr co-existed in molten KCl–$MgCl_2$, δ-A15 Cr appears to be more stable than bcc Cr under these conditions, because the amount of bcc Cr decreased continuously. The formation of δ-A15 and pores has led to a decrease in the coordination number of Cr–Cr, however the bond length did not change significantly.

The surface energy for different facets of bcc and δ-A15 Cr was simulated. The thermodynamics from 0–1000 K were also calculated for both phases. KCl adsorption energies were computed with DFT to initially probe the influence of molten KCl–$MgCl_2$ on both phases. Though bcc Cr is more stable at room temperature, its relative stability decreases at higher temperature. Furthermore, the (200) facet of δ-A15 Cr exhibits a comparable KCl adsorption energy to that of (110)-bcc Cr and a significantly greater KCl adsorption energy than (100)-bcc Cr. AIMD simulations of a 50–50 mol% mixture of molten KCl–$MgCl_2$ on (110)-bcc and (200)-δ-A15 Cr surfaces revealed differing interfacial behaviors in the molten salt. The (200)-δ-A15 Cr surface exhibits greater coordination of Mg^{2+} and Cl^- with surface Cr atoms than on (110)-bcc Cr. Notably, Mg^{2+} approaches the surface of (200)-δ-A15 Cr more closely and exhibits significantly less lateral mobility (*i.e.*, surface diffusion) than on (110)-bcc Cr, which suggests stronger ion-surface interactions for (200)-δ-A15 Cr. Thus, the simulations have identified multiple factors that support the appearance of δ-A15 Cr in a KCl–$MgCl_2$ molten salt environment.

In summary, this work was motivated by the importance of understanding solid–liquid interfaces with highly reactive media, which critically determine the properties of materials in a wide range of applications. The research presented here focuses on the interfacial evolution of Cr microparticles in molten salts, a model system for investigating real-time reactions under extreme conditions. By employing a synchrotron multimodal approach, including nano-tomography, absorption spectroscopy, and diffraction, along with density functional theory and *ab initio* molecular dynamics simulations, a comprehensive investigation framework was established. The results

revealed intriguing interfacial phase transformation phenomena, such as the dissolution of Cr and the formation of δ-Cr, leading to changes in the Cr coordination environment in the molten salt. The proposed strategy offers valuable insights and characterization tools applicable to a wide range of materials and their interactions with reactive fluids. This research contributes to the advancement of sustainable energy applications, such as solar and nuclear power plants, colloidal and two-dimensional materials synthesis, and batteries, and opens new possibilities for understanding and potentially tailoring solid–liquid interfacial properties in various technological fields.

Data availability statement

The digital data for all figures, tables, charts, and any other media contained in this publication and its associated ESI† files will be made accessible on the Zenodo repository, under Digital Object Identifier (DOI): **https://doi.org/10.5281/zenodo.7842785**.

Funding statement

Funding was provided by the U.S. Department of Energy Office of Science, Office of Basic Energy Sciences under contracts DE-SC0012704 and DE-AC05-00OR22725.

Conflicts of interest

The authors declare no competing interests.

Acknowledgements

This work was supported as part of the Molten Salts in Extreme Environments (MSEE) Energy Frontier Research Center, funded by the U.S. Department of Energy, Office of Science, Basic Energy Sciences. BNL and ORNL are operated under DOE contracts DE-SC0012704 and DE-AC05-00OR22725, respectively. Work at Stony Brook University was supported by MSEE through a subcontract from BNL. This research used resources, the 8-ID (ISS), 18-ID (FXI), 28-ID-1 (PDF) and 28-ID-2 (XPD) beamlines of the National Synchrotron Light Source II, a U.S. Department of Energy (DOE) Office of Science User Facility operated for the DOE Office of Science by Brookhaven National Laboratory under Contract DE-SC0012704. This research used resources of the Center for Functional Nanomaterials, which is a U.S. DOE Office of Science Facility at Brookhaven National Laboratory under Contract No. DE-SC0012704. This research used resources of the Oak Ridge Leadership Computing Facility at the Oak Ridge National Laboratory, which is supported by the Office of Science of the U.S. Department of Energy under Contract No. DE-AC05-00OR22725, as well as resources of the National Energy Research Scientific Computing Center (NERSC), a U.S. Department of Energy Office of Science User Facility located at Lawrence Berkeley National Laboratory, operated under Contract DE-AC02-05CH11231 using NERSC award NP-ERCAP0020487. The authors thank Dr Eli Stavitski, the lead scientist of the ISS beamline. The authors thank Lin-Chieh Yu for conducting the SEM analysis. Current and former Chen-Wiegart group members – Arthur Ronne, Dean Yen, and Chonghang Zhao are acknowledged for conducting the beamtime experiments together at the FXI beamline.

References

1 F. Polo-Garzon, Z. H. Bao, X. Y. Zhang, W. X. Huang and Z. L. Wu, Surface Reconstructions of Metal Oxides and the Consequences on Catalytic Chemistry, *ACS Catal.*, 2019, **9**, 5692–5707.
2 Z. J. Bi, Q. F. Sun, M. Y. Jia, M. X. Zuo, N. Zhao and X. X. Guo, Molten Salt Driven Conversion Reaction Enabling Lithiophilic and Air-Stable Garnet Surface for Solid-State Lithium Batteries, *Adv. Funct. Mater.*, 2022, **32**, 2208751.
3 H. Liu, X. Zhang, S. M. He, D. He, Y. Shang and H. J. Yu, Molten salts for rechargeable batteries br, *Mater. Today*, 2022, **60**, 128–157.
4 R. Cheula, M. D. Susman, D. H. West, S. Chinta, J. D. Rimer and M. Maestri, Local Ordering of Molten Salts at NiO Crystal Interfaces Promotes High-Index Faceting, *Angew. Chem., Int. Ed.*, 2021, **60**, 25391–25396.
5 H. Zhang, K. Dasbiswas, N. B. Ludwig, G. Han, B. Lee, S. Vaikuntanathan and D. V. Talapin, Stable colloids in molten inorganic salts, *Nature*, 2017, **542**, 328.
6 Z. Zhu, D. W. Yu, Y. Yang, C. Su, Y. M. Huang, Y. H. Dong, I. Waluyo, B. M. Wang, A. Hunt, X. H. Yao, J. Lee, W. J. Xue and J. Li, Gradient Li-rich oxide cathode particles immunized against oxygen release by a molten salt treatment, *Nat. Energy*, 2019, **4**, 1049–1058.
7 V. Kamysbayev, A. S. Filatov, H. C. Hu, X. Rui, F. Lagunas, D. Wang, R. F. Klie and D. V. Talapin, Covalent surface modifications and superconductivity of two-dimensional metal carbide MXenes, *Science*, 2020, **369**, 979.
8 E. T. Dias, S. K. Gill, Y. Liu, P. Halstenberg, S. Dai, J. H. Huang, J. Mausz, R. Gakhar, W. C. Phillips, S. Mahurin, S. M. Pimblott, J. F. Wishart and A. I. Frenkel, Radiation-Assisted Formation of Metal Nanoparticles in Molten Salts, *J. Phys. Chem. Lett.*, 2021, **12**, 157–164.
9 T. T. Niu, L. F. Chao, W. Y. Gao, C. X. Ran, L. Song, Y. H. Chen, L. Fu and W. Huang, Ionic Liquids-Enabled Efficient and Stable Perovskite Photovoltaics: Progress and Challenges, *ACS Energy Lett.*, 2021, **6**, 1453–1479.
10 J. Serp, M. Allibert, O. Benes, S. Delpech, O. Feynberg, V. Ghetta, D. Heuer, D. Holcomb, V. Ignatiev, J. L. Kloosterman, L. Luzzi, E. Merle-Lucotte, J. Uhlir, R. Yoshioka and Z. M. Dai, The molten salt reactor (MSR) in generation IV: Overview and perspectives, *Prog. Nucl. Energy*, 2014, **77**, 308–319.
11 J. Mcmurray, K. Johnson, C. Agca, B. Betzler, D. Kropaczek, T. Besmann, D. Andersson and N. Dianne Ezell, *Roadmap for thermal property measurements of Molten Salt Reactor systems*, 2021.
12 D. F. Williams and K. T. Clarno, Evaluation of salt coolants for reactor applications, *Nucl. Technol.*, 2008, **163**, 330–343.

13 Q. J. Li, E. Küçükbenli, S. Lam, B. Khaykovich, E. Kaxiras and J. Li, Development of robust neural-network interatomic potential for molten salt, *Cell Rep. Phys. Sci.*, 2021, **2**, 100359.
14 S. Bell, T. Steinberg and G. Will, Corrosion mechanisms in molten salt thermal energy storage for concentrating solar power, *Renewable Sustainable Energy Rev.*, 2019, **114**, 109328.
15 H. L. Zhang, J. Baeyens, J. Degrève and G. Cacères, Concentrated solar power plants: Review and design methodology, *Renewable Sustainable Energy Rev.*, 2013, **22**, 466–481.
16 S. Kuravi, J. Trahan, D. Y. Goswami, M. M. Rahman and E. K. Stefanakos, Thermal energy storage technologies and systems for concentrating solar power plants, *Prog. Energy Combust. Sci.*, 2013, **39**, 285–319.
17 N. Lin, Y. Han, J. Zhou, K. L. Zhang, T. J. Xu, Y. C. Zhu and Y. T. Qian, A low temperature molten salt process for aluminothermic reduction of silicon oxides to crystalline Si for Li-ion batteries, *Energy Environ. Sci.*, 2015, **8**, 3187–3191.
18 J. L. Lang, K. Liu, Y. Jin, Y. Z. Long, L. H. Qi, H. Wu and Y. Cui, A molten battery consisting of Li metal anode, AlCl3-LiCl cathode and solid electrolyte, *Energy Storage Mater.*, 2020, **24**, 412–416.
19 M. Li, J. Lu, K. Luo, Y. B. Li, K. K. Chang, K. Chen, J. Zhou, J. Rosen, L. Hultman, P. Eklund, P. Persson, S. Y. Du, Z. F. Chai, Z. R. Huang and Q. Huang, Element Replacement Approach by Reaction with Lewis Acidic Molten Salts to Synthesize Nanolaminated MAX Phases and MXenes, *J. Am. Chem. Soc.*, 2019, **141**, 4730–4737.
20 Y. B. Li, H. Shao, Z. F. Lin, J. Lu, L. Y. Liu, B. Duployer, P. Persson, P. Eklund, L. Hultman, M. Li, K. Chen, X. H. Zha, S. Y. Du, P. Rozier, Z. F. Chai, E. Raymundo-Piñero, P. L. Taberna, P. Simon and Q. Huang, A general Lewis acidic etching route for preparing MXenes with enhanced electrochemical performance in non-aqueous electrolyte, *Nat. Mater.*, 2020, **19**, 894.
21 M. M. Li, X. W. Zhan, E. Polikarpov, N. L. Canfield, M. H. Engelhard, J. M. Weller, D. M. Reed, V. L. Sprenkle and G. S. Li, A freeze-thaw molten salt battery for seasonal storage, *Cell Rep. Phys. Sci.*, 2022, **3**, 100821.
22 K. Baek, W. C. Jeon, S. Woo, J. C. Kim, J. G. Lee, K. An, S. K. Kwak and S. J. Kang, Synergistic effect of quinary molten salts and ruthenium catalyst for high-power-density lithium-carbon dioxide cell, *Nat. Commun.*, 2020, **11**, 456.
23 V. Giordani, D. Tozier, H. J. Tan, C. M. Burke, B. M. Gallant, J. Uddin, J. R. Greer, B. D. McCloskey, G. V. Chase and D. Addison, A Molten Salt Lithium-Oxygen Battery, *J. Am. Chem. Soc.*, 2016, **138**, 2656–2663.
24 N. Díez, A. B. Fuertes and M. Sevilla, Molten salt strategies towards carbon materials for energy storage and conversion, *Energy Storage Mater.*, 2021, **38**, 50–69.
25 T. Ghaznavi, S. Y. Persaud and R. C. Newman, Electrochemical Corrosion Studies in Molten Chloride Salts, *J. Electrochem. Soc.*, 2022, **169**, 061502.
26 T. Ghaznavi, M. A. Bryk, S. Y. Persaud and R. C. Newman, Alloying effects in high temperature molten salt corrosion, *Corros. Sci.*, 2022, **197**, 110003.
27 X. Y. Liu, A. Ronne, L. C. Yu, Y. Liu, M. Y. Ge, C. H. Lin, B. Layne, P. Halstenberg, D. S. Maltsev, A. S. Ivanov, S. Antonelli, S. Dai, W. K. Lee, S. M. Mahurin, A. I. Frenkel, J. F. Wishart, X. H. Xiao and Y. Chen-Wiegart, Formation of three-dimensional bicontinuous structures via molten salt dealloying studied in real-time by *in situ* synchrotron X-ray nano-tomography, *Nat. Commun.*, 2021, **12**, 1006–1018.
28 X. F. Liu, N. Fechler and M. Antonietti, Salt melt synthesis of ceramics, semiconductors and carbon nanostructures, *Chem. Soc. Rev.*, 2013, **42**, 8237–8265.
29 X. F. Liu, M. Antonietti and C. Giordano, Manipulation of Phase and Microstructure at Nanoscale for SiC in Molten Salt Synthesis, *Chem. Mater.*, 2013, **25**, 2021–2027.
30 T. Li, Y. Xu, X. Qian, Q. Yue and Y. J. Kang, Low-Temperature Molten Salt Synthesis for Ligand-Free Transition Metal Oxide Nanoparticles, *ACS Appl. Energy Mater.*, 2020, **3**, 3984–3990.
31 A. H. Bork, N. Ackerl, J. Reuteler, S. Jog, D. Gut, R. Zboray and C. R. Muller, Model structures of molten salt-promoted MgO to probe the mechanism of MgCO3 formation during CO2 capture at a solid-liquid interface, *J. Mater. Chem. A*, 2022, **10**, 16803–16812.
32 M. R. M. K. Y.-H. W. A. K. F. Donat and P. M. A. C. R. Müller, Deciphering the structural dynamics in molten salt–promoted MgO-based CO_2 sorbents and their role in the CO_2 uptake, *Sci. Adv.*, 2023, **9**, eadg5690.
33 X. W. Fei Liang, W. Wang, J. Ding and S. Liu, MgO/Molten salt interfacial thermal transport and its consequences on thermophysical property enhancement: A molecular dynamics study, *Int. J. Heat Mass Transfer*, 2023, **207**, 124022.
34 Y. S. Wang, X. Q. Yu, S. Y. Xu, J. M. Bai, R. J. Xiao, Y. S. Hu, H. Li, X. Q. Yang, L. Q. Chen and X. J. Huang, A zero-strain layered metal oxide as the negative electrode for long-life sodium-ion batteries, *Nat. Commun.*, 2013, **4**, 2365.
35 X. K. Xu, X. X. Wang, P. W. Li, Y. Y. Li, Q. Hao, B. Xiao, H. Elsentriecy and D. Gervasio, Experimental Test of Properties of KCl-MgCl2 Eutectic Molten Salt for Heat Transfer and Thermal Storage Fluid in Concentrated Solar Power Systems, *J. Sol. Energy Eng.*, 2018, **140**, 051011.
36 N. A. Anderson and P. Sabharwall, Molten Salt Mixture Properties (Kf-Zrf4 And Kcl-Mgcl2) For Use In Relap5-3d For High-Temperature Reactor Application, *Nucl. Technol.*, 2012, **178**, 335–340.
37 K. Hanson, K. M. Sankar, P. F. Weck, J. K. Startt, R. Dingreville, C. S. Deo, J. D. Sugar and P. M. Singh, Effect of excess Mg to control corrosion in molten MgCl2 and KCl eutectic salt mixture, *Corros. Sci.*, 2022, **194**, 109914.
38 S. Q. Guo, J. S. Zhang, W. Wu and W. T. Zhou, Corrosion in the molten fluoride and chloride salts and materials development for nuclear applications, *Prog. Mater. Sci.*, 2018, **97**, 448–487.
39 G. Q. Zheng and K. Sridharan, Corrosion of Structural Alloys in High-Temperature Molten Fluoride Salts for Applications in Molten Salt Reactors, *JOM*, 2018, **70**, 1535–1541.

40 S. S. Raiman and S. Lee, Aggregation and data analysis of corrosion studies in molten chloride and fluoride salts, *J. Nucl. Mater.*, 2018, **511**, 523–535.
41 S. W. McAlpine, N. C. Skowronski, W. Y. Zhou, G. Q. Zheng and M. P. Short, Corrosion of commercial alloys in FLiNaK molten salt containing EuF3 and simulant fission product additives, *J. Nucl. Mater.*, 2020, **532**, 151994.
42 A. B. Wenjin Ding and T. Bauer, Development of molten chloride salts for thermal energy storage in next generation concentrated solar power (CSP) plants, International Forum on Advanced Materials (IFAM), 2018, **https://elib.dlr.de/125794/**.
43 Y. F. Wang, B. Goh, P. Nelaturu, T. Duong, N. Hassan, R. David, M. Moorehead, S. Chaudhuri, A. Creuziger, J. Hattrick-Simpers, D. J. Thoma, K. Sridharan and A. Couet, Integrated High-Throughput and Machine Learning Methods to Accelerate Discovery of Molten Salt Corrosion-Resistant Alloys, *Adv. Sci.*, 2022, **9**, 2200370.
44 K. Bawane, X. Y. Liu, R. Gakhar, M. Woods, M. Y. Ge, X. H. Xiao, W. K. Lee, P. Halstenberg, S. Dai, S. Mahurin, S. M. Pimblott, J. F. Wishart, Y. C. K. Chen-Wiegart and L. F. He, Visualizing time-dependent microstructural and chemical evolution during molten salt corrosion of Ni-20Cr model alloy using correlative quasi *in situ* TEM and *in situ* synchrotron X-ray nano-tomography, *Corros. Sci.*, 2022, **195**, 109962.
45 A. Ronne, L. F. He, D. Dolzhnikov, Y. Xie, M. Y. Ge, P. Halstenberg, Y. C. Wang, B. T. Manard, X. H. Xiao, W. K. Lee, K. Sasaki, S. Dai, S. M. Mahurin and Y. C. K. Chen-Wiegart, Revealing 3D Morphological and Chemical Evolution Mechanisms of Metals in Molten Salt by Multimodal Microscopy, *ACS Appl. Mater. Interfaces*, 2020, **12**, 17321–17333.
46 S. K. Gill, J. Sure, Y. C. Wang, B. Layne, L. F. He, S. Mahurin, J. F. Wishart and K. Sasaki, Investigating corrosion behavior of Ni and Ni-20Cr in molten ZnCl2, *Corros. Sci.*, 2021, **179**, 109105.
47 Y. Yang, W. Y. Zhou, S. Yin, S. Y. Wang, Q. Yu, M. J. Olszta, Y. Q. Zhang, S. E. Zeltmann, M. D. Li, M. M. Jin, D. K. Schreiber, J. Ciston, M. C. Scott, J. R. Scully, R. O. Ritchie, M. Asta, J. Li, M. P. Short and A. M. Minor, One dimensional wormhole corrosion in metals, *Nat. Commun.*, 2023, **14**, 988.
48 S. Roy, S. Sharma, W. V. Karunaratne, F. Wu, R. Gakhar, D. S. Maltsev, P. Halstenberg, M. Abeykoon, S. K. Gill, Y. P. Zhang, S. M. Mahurin, S. Dai, V. S. Bryantsev, C. J. Margulis and A. S. Ivanov, X-ray scattering reveals ion clustering of dilute chromium species in molten chloride medium, *Chem. Sci.*, 2021, **12**, 8026–8035.
49 Q. J. Li, D. Sprouster, G. Q. Zheng, J. C. Neuefeind, A. D. Braatz, J. McFarlane, D. Olds, S. Lam, J. Li and B. Khaykovich, Complex Structure of Molten NaCl-CrCl3 Salt: Cr-Cl Octahedral Network and Intermediate-Range Order, *ACS Appl. Energy Mater.*, 2021, **4**, 3044–3056.
50 S. Roy, Y. Liu, M. Topsakal, E. Dias, R. Gakhar, W. C. Phillips, J. F. Wishart, D. Leshchev, P. Halstenberg, S. Dai, S. K. Gill, A. I. Frenkel and V. S. Bryantsev, A Holistic Approach for Elucidating Local Structure, Dynamics, and Speciation in Molten Salts with High Structural Disorder, *J. Am. Chem. Soc.*, 2021, **143**, 15298–15308.
51 K. Bawane, P. Manganaris, Y. C. Wang, J. Sure, A. Ronne, P. Halstenberg, S. Dai, S. K. Gill, K. Sasaki, Y. C. K. Chen-Wiegart, R. Gakhar, S. Mahurin, S. M. Pimblott, J. F. Wishart and L. F. He, Determining oxidation states of transition metals in molten salt corrosion using electron energy loss spectroscopy, *Scr. Mater.*, 2021, **197**, 113790.
52 Y. X. Peng, P. S. Shinde and R. G. Reddy, High-temperature corrosion rate and diffusion modelling of Ni-coated incoloy 800H alloy in $MgCl_2$–KCl heat transfer fluid, *Sol. Energy Mater. Sol. Cells*, 2022, **243**, 111767.
53 B. D'Souza, A. Leong, Q. F. Yang and J. S. Zhang, Corrosion behavior of boronized nickel-based alloys in the molten chloride Salt, *Corros. Sci.*, 2021, **182**, 109285.
54 X. Liu, K. Bawane, X. Zheng, M. Ge, P. Halstenberg, D. S. Maltsev, A. S. Ivanov, S. Dai, X. Xiao, W.-K. Lee, L. He and Y.-C. K. Chen-Wiegart, Temperature-Dependent Morphological Evolution during Corrosion of the Ni-20Cr Alloy in Molten Salt Revealed by Multiscale Imaging, *ACS Appl. Mater. Interfaces*, 2023, **15**, 13772–13782.
55 Y. K. Kazuo Kimoto, M. Nonoyama and R. Uyeda, An Electron Microscope Study on Fine Metal Particles Prepared by Evaporation in Argon Gas at Low Pressure, *Jpn. J. Appl. Phys.*, 1963, **2**, 702.
56 K. Kimoto and I. Nishida, An Electron Diffraction Study On Crystal Structure Of A New Modification Of Chromium, *J. Phys. Soc. Jpn.*, 1967, **22**, 744.
57 M. I. Birjega and N. Popescupogrion, On The Relations Between The Delta-Cr And Alpha-Cr Phases, *Thin Solid Films*, 1989, **171**, 33–41.
58 J. Forssell and B. Persson, Growth And Structure Of Thin Chromium Films Condensed On Ultra-High Vacuum Cleaved Nacl And Kcl Crystals, *J. Phys. Soc. Jpn.*, 1970, **29**, 1532.
59 J. P. Chu, J. W. Chang, P. Y. Lee, J. K. Wu and J. Y. Wang, On the formation of nonequilibrium A15 crystal structure chromium thin films by sputter deposition, *Thin Solid Films*, 1998, **312**, 78–85.
60 I. Nishida and K. Kimoto, Crystal Habit And Crystal-Structure Of Fine Chromium Particles - Electron-Microscope And Electron-Diffraction Study Of Fine Metallic Particles Prepared By Evaporation In Argon At Low-Pressures (III), *Thin Solid Films*, 1974, **23**, 179–189.
61 M. Idrees, S. M. Abbas, R. Ata Ur, N. Ahmad, M. W. Mushtaq, R. A. Naqvi, K. W. Nam, B. Muhammad and Z. Iqbal, Mechanistic insights into high lithium storage performance of mesoporous chromium nitride anchored on nitrogen- doped carbon nanotubes, *Chem. Eng. J.*, 2017, **327**, 361–370.
62 Q. Sun and Z. W. Fu, An anode material of CrN for lithium-ion batteries, *Electrochem. Solid-State Lett.*, 2007, **10**, A189–A193.
63 A. I. Frenkel, C. W. Hills and R. G. Nuzzo, A view from the inside: Complexity in the atomic scale ordering of supported metal nanoparticles, *J. Phys. Chem. B*, 2001, **105**, 12689–12703.

64 L. Li, L. L. Wang, D. D. Johnson, Z. F. Zhang, S. I. Sanchez, J. H. Kang, R. G. Nuzzo, Q. Wang, A. I. Frenkel, J. Li, J. Ciston, E. A. Stach and J. C. Yang, Noncrystalline-to-Crystalline Transformations in Pt Nanoparticles, *J. Am. Chem. Soc.*, 2013, **135**, 13062–13072.
65 Y. L. Wang, Q. Wang, H. J. Liu and C. L. Zeng, Effects of the oxidants H2O and CrF3 on the corrosion of pure metals in molten (Li,Na,K)F, *Corros. Sci.*, 2016, **103**, 268–282.
66 W. Y. Zhou, Y. Yang, G. Q. Zheng, K. B. Woller, P. W. Stahle, A. M. Minor and M. P. Short, Proton irradiation-decelerated intergranular corrosion of Ni-Cr alloys in molten salt, *Nat. Commun.*, 2020, **11**, 3430.
67 S. Matsuo and I. Nishida, Magnetic-Properties Of A New Magnetic Phase In Fine Bcc Chromium Particles Prepared By Gas Evaporation Method, *J. Phys. Soc. Jpn.*, 1980, **49**, 1005–1012.
68 M. P. J. Punkkinen, Q. M. Hu, S. K. Kwon, B. Johansson, J. Kollár and L. Vitos, Surface properties of 3d transition metals, *Philos. Mag.*, 2011, **91**, 3627–3640.
69 L. M. Corliss, J. M. Hastings and R. J. Weiss, Antiphase Antiferromagnetic Structure of Chromium, *Phys. Rev. Lett.*, 1959, **3**, 211–212.
70 J. Chen, H. Krakauer and D. J. Singh, Surface Strain of Tungsten (001), *Phys. Rev. B: Condens. Matter Mater. Phys.*, 1991, **43**, 2398–2400.
71 S. Antonelli, A. Ronne, I. Han, M. Y. Ge, B. Layne, A. J. Shahani, K. Iwamatsu, J. F. Wishart, S. L. Hulbert, W. K. Lee, Y. C. K. Chen-Wiegart and X. H. Xiao, Versatile compact heater design for *in situ* nano-tomography by transmission X-ray microscopy, *J. Synchrotron Radiat.*, 2020, **27**, 746–752.
72 D. Gursoy, F. De Carlo, X. H. Xiao and C. Jacobsen, TomoPy: a framework for the analysis of synchrotron tomographic data, *J. Synchrotron Radiat.*, 2014, **21**, 1188–1193.
73 C. Prescher and V. B. Prakapenka, DIOPTAS: a program for reduction of two-dimensional X-ray diffraction data and data exploration, *High Press. Res.*, 2015, **35**, 223–230.
74 B. Ravel and M. Newville, ATHENA, ARTEMIS, HEPHAESTUS: data analysis for X-ray absorption spectroscopy using IFEFFIT, *J. Synchrotron Radiat.*, 2005, **12**, 537–541.
75 A. I. Frenkel, D. M. Pease, J. I. Budnick, P. Shanthakumar and T. Huang, Application of glancing-emergent-angle fluorescence for polarized XAFS studies of single crystals, *J. Synchrotron Radiat.*, 2007, **14**, 272–275.
76 G. Kresse and J. Furthmuller, Efficiency of ab-initio total energy calculations for metals and semiconductors using a plane-wave basis set, *Comput. Mater. Sci.*, 1996, **6**, 15–50.
77 G. Kresse and J. Furthmuller, Efficient iterative schemes for ab initio total-energy calculations using a plane-wave basis set, *Phys. Rev. B: Condens. Matter Mater. Phys.*, 1996, **54**, 11169–11186.
78 G. Kresse and J. Hafner, Ab-Initio Molecular-Dynamics Simulation Of The Liquid-Metal Amorphous-Semiconductor Transition In Germanium, *Phys. Rev. B: Condens. Matter Mater. Phys.*, 1994, **49**, 14251–14269.
79 G. Kresse and J. Hafner, Ab-Initio Molecular-Dynamics For Open-Shell Transition-Metals, *Phys. Rev. B: Condens. Matter Mater. Phys.*, 1993, **48**, 13115–13118.
80 J. P. Perdew, K. Burke and M. Ernzerhof, Generalized gradient approximation made simple, *Phys. Rev. Lett.*, 1997, **78**, 1396.
81 J. P. Perdew, K. Burke and M. Ernzerhof, Comment on ''Generalized gradient approximation made simple'' - Reply, *Phys. Rev. Lett.*, 1998, **80**, 891.
82 M. Ropo, K. Kokko and L. Vitos, Assessing the Perdew-Burke-Ernzerhof exchange-correlation density functional revised for metallic bulk and surface systems, *Phys. Rev. B: Condens. Matter Mater. Phys.*, 2008, **77**, 195445.
83 G. Y. Guo and H. H. Wang, Calculated elastic constants and electronic and magnetic properties of bcc, fcc, and hcp Cr crystals and thin films, *Phys. Rev. B: Condens. Matter Mater. Phys.*, 2000, **62**, 5136–5143.
84 R. Soulairol, C. C. Fu and C. Barreteau, Structure and magnetism of bulk Fe and Cr: from plane waves to LCAO methods, *J. Phys.: Condens. Matter*, 2010, **22**, 295502.
85 R. Hafner, D. Spisák, R. Lorenz and J. Hafner, Magnetic ground state of Cr in density-functional theory, *Phys. Rev. B: Condens. Matter Mater. Phys.*, 2002, **65**, 184432.
86 A. S. Belozerov, A. A. Katanin and V. I. Anisimov, Itinerant magnetism of chromium under pressure: a DFT plus DMFT study, *J. Phys.: Condens. Matter*, 2021, **33**, 385601.
87 B. G. Janesko, Replacing hybrid density functional theory: motivation and recent advances, *Chem. Soc. Rev.*, 2021, **50**, 8470–8495.
88 J. Hubbard, Electron Correlations in Narrow Energy Bands, *Proc. R. Soc. London, Ser. A*, 1963, **276**, 238–257.
89 P. W. Anderson, Localized Magnetic States in Metals, *Phys. Rev.*, 1961, **124**, 41–53.
90 R. Shinde, S. Yamijala and B. M. Wong, Improved band gaps and structural properties from Wannier-Fermi-Lowdin self-interaction corrections for periodic systems, *J. Phys.: Condens. Matter*, 2021, **33**, 115501.
91 A. Togo and I. Tanaka, First principles phonon calculations in materials science, *Scr. Mater.*, 2015, **108**, 1–5.

